

Supporting Online Material for Fleitmann *et al.*

Supporting Tables

Table S1: Results of TIMS U/Th dating

| Sample | depth [mm] | c(Th-230) | | c(Th-232) | | c(U-234) | | c(U-238) | | delta U-234 | | Age | |
|--------|---------------|-----------|-------|-----------|-------|----------|--------|----------|--------|-------------|------|--------|---------|
| | | [pg/g] | ± | [ng/g] | ± | [ng/g] | ± | [µg/g] | ± | [‰] | ± | [kyr] | ± [kyr] |
| Q5 | 2 | 0.033 | 0.002 | 1.660 | 0.012 | 0.023 | 0.0001 | 0.457 | 0.0022 | -55.1 | 6.0 | 0.400 | 0.024 |
| Q5 | 62.3 | 0.214 | 0.003 | 2.688 | 0.020 | 0.025 | 0.0001 | 0.488 | 0.0009 | -63.9 | 3.4 | 3.010 | 0.057 |
| Q5 | 140 | 0.300 | 0.009 | 0.777 | 0.007 | 0.029 | 0.0001 | 0.587 | 0.0012 | -81.1 | 3.8 | 3.740 | 0.129 |
| Q5 | 197 | 0.258 | 0.007 | 0.768 | 0.010 | 0.025 | 0.0001 | 0.490 | 0.0010 | -67.3 | 6.0 | 3.790 | 0.138 |
| Q5 | 259 | 0.339 | 0.013 | 2.998 | 0.069 | 0.027 | 0.0005 | 0.544 | 0.0035 | -65.1 | 19.2 | 4.380 | 0.265 |
| Q5 | 340 | 0.342 | 0.006 | 0.376 | 0.003 | 0.029 | 0.0001 | 0.579 | 0.0011 | -82.3 | 4.4 | 4.370 | 0.105 |
| Q5 | 428 | 0.390 | 0.008 | 2.374 | 0.021 | 0.029 | 0.0001 | 0.570 | 0.0011 | -70.2 | 4.7 | 4.900 | 0.136 |
| Q5 | 503 | 0.475 | 0.008 | 0.580 | 0.005 | 0.030 | 0.0002 | 0.617 | 0.0014 | -85.8 | 5.0 | 5.750 | 0.134 |
| Q5 | 574 | 0.538 | 0.012 | 1.223 | 0.011 | 0.030 | 0.0001 | 0.608 | 0.0013 | -77.1 | 4.8 | 6.540 | 0.183 |
| Q5 | 702 | 0.732 | 0.016 | 1.638 | 0.038 | 0.034 | 0.0001 | 0.696 | 0.0017 | -86.7 | 3.5 | 7.910 | 0.213 |
| Q5 | 780 | 1.135 | 0.023 | 38.85 | 0.416 | 0.041 | 0.0001 | 0.817 | 0.0024 | -58.0 | 3.9 | 8.870 | 0.232 |
| Q5 | 860 | 2.046 | 0.022 | 0.390 | 0.003 | 0.079 | 0.0003 | 1.585 | 0.0033 | -76.7 | 3.7 | 9.760 | 0.155 |
| Q5 | 903 | 2.062 | 0.030 | 0.940 | 0.009 | 0.077 | 0.0003 | 1.571 | 0.0037 | -88.8 | 4.6 | 10.060 | 0.210 |
| Q5 | 961 | 2.481 | 0.030 | 0.270 | 0.002 | 0.089 | 0.0002 | 1.827 | 0.0035 | -90.9 | 2.8 | 10.470 | 0.170 |
| S4 | 3 | 0.867 | 0.008 | 3.227 | 0.007 | 0.030 | 0.0001 | 0.605 | 0.0020 | 87.4 | 3.4 | 9.020 | 0.103 |
| S4 | 87 | 0.542 | 0.007 | 1.787 | 0.013 | 0.022 | 0.0001 | 0.387 | 0.0010 | 49.4 | 4.7 | 9.150 | 0.168 |
| S4 | 112 | 0.567 | 0.008 | 1.626 | 0.013 | 0.022 | 0.0001 | 0.388 | 0.0009 | 57.6 | 5.4 | 9.520 | 0.193 |
| S4 | 209 | 0.637 | 0.006 | 2.683 | 0.005 | 0.028 | 0.0001 | 0.418 | 0.0010 | 53.5 | 3.8 | 9.930 | 0.202 |
| S4 | 400 | 0.951 | 0.019 | 4.536 | 0.045 | 0.033 | 0.0002 | 0.595 | 0.0014 | 35.4 | 6.8 | 10.600 | 0.299 |

Table S2: Results of MC-ICPMS U/Th dating

| Sample | depth [mm] | c(Th) | | c(U) | | $(^{234}\text{U}/^{238}\text{U})$ | | $(^{230}\text{Th}/^{232}\text{Th})$ | | $(^{230}\text{Th}/^{234}\text{U})$ | | Age | |
|--------|---------------|-------|-------|-------|-----|-----------------------------------|--------|-------------------------------------|-------|------------------------------------|---------|-------|-------|
| | | [ppb] | ± | [ppb] | ± | ± | ± | ± | ± | [kyr] | ± [kyr] | | |
| Q5 | 40 | 2.164 | 0.012 | 664.9 | 1.8 | 0.9348 | 0.0007 | 11.83 | 0.14 | 0.0136 | 0.0002 | 1.400 | 0.030 |
| Q5 | 565 | 3.334 | 0.022 | 606.3 | 1.6 | 0.9149 | 0.0010 | 28.88 | 0.32 | 0.0575 | 0.0005 | 6.470 | 0.090 |
| Q5 | 627 | 1.641 | 0.009 | 632.9 | 1.6 | 0.9275 | 0.0008 | 66.58 | 0.58 | 0.0616 | 0.0005 | 6.960 | 0.080 |
| Q5 | 762 | 0.449 | 0.003 | 676.2 | 1.7 | 0.9132 | 0.0009 | 324.13 | 3.58 | 0.078 | 0.0008 | 8.880 | 0.120 |
| Q11 | 14 | 0.944 | 0.005 | 288.3 | 0.7 | 1.0288 | 0.0013 | 32.69 | 0.48 | 0.03447 | 0.00048 | 3.738 | 0.080 |
| Q11 | 102 | 1.499 | 0.021 | 216.3 | 0.6 | 1.0267 | 0.0010 | 6.32 | 18.81 | 0.04207 | 0.00058 | 4.501 | 0.080 |
| Q11 | 176 | 0.315 | 0.002 | 231.1 | 0.6 | 1.0212 | 0.0015 | 14.47 | 99.79 | 0.04414 | 0.00045 | 4.929 | 0.080 |

Supporting Figures

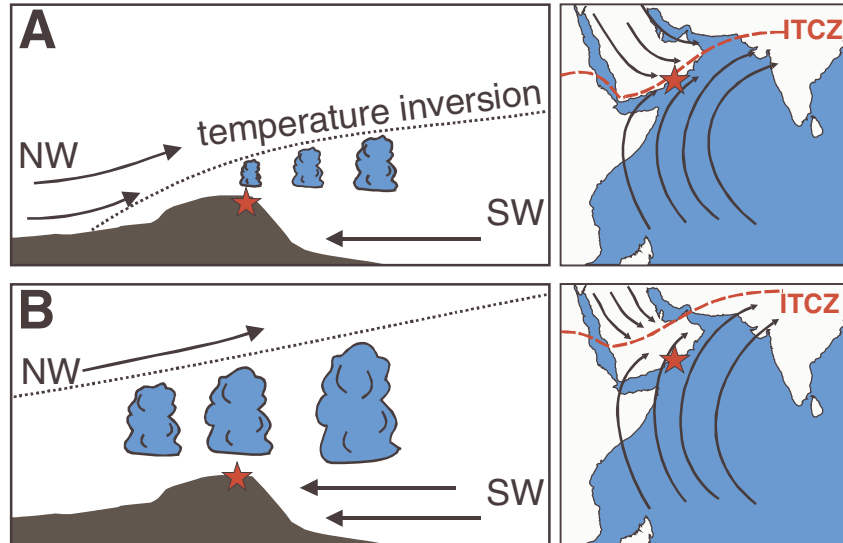


Figure S1. (A) Schematic figure of modern summer circulation pattern over Southern Oman. The red star shows the location of Qunf Cave. The black dashed line shows the position of the temperature inversion and the red dashed line the location of the ITCZ. (B) Schematic figure of summer circulation pattern at around 7 kyr BP.

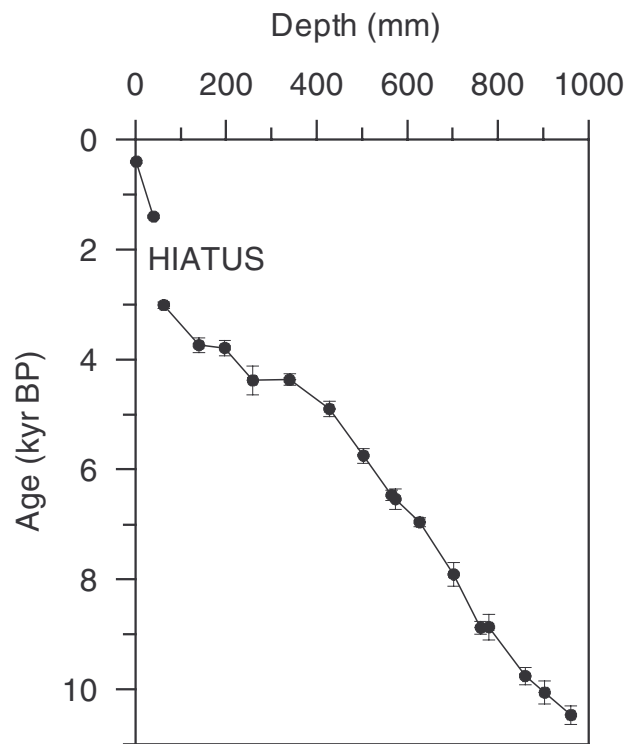


Figure S2. Plot of age versus depth for stalagmite Q5 (see Tables S1 and S2 for further details).

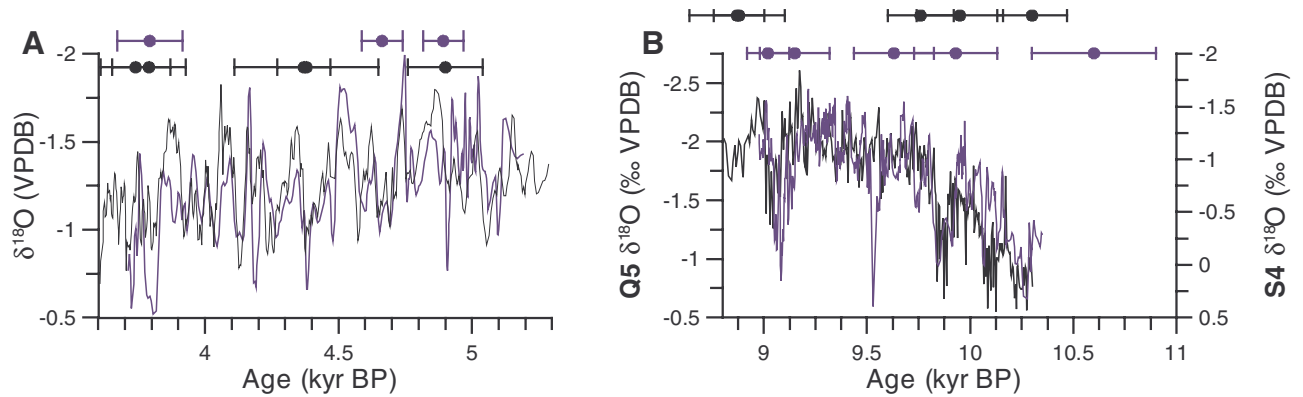


Figure S3. (A) Comparison of smoothed (3 point running average) $\delta^{18}\text{O}$ profiles of stalagmites Q5 (black line) and Q11 (blue line) from Qunf Cave, and (B) of stalagmites Q5 (black line) and S4 (blue line). Stalagmite S4 was sampled in Kahf Defore (~150 m above sea level), approximately 40 km apart from Qunf Cave. Age calibration of stalagmite S4 is based on Th-U ages and annual growth band counts. The overall difference in $\delta^{18}\text{O}$ between Q5 and S4 is caused by the altitude effect, which accounts for the observed difference of ~0.7‰. Error bars are color-coded Th-U ages.

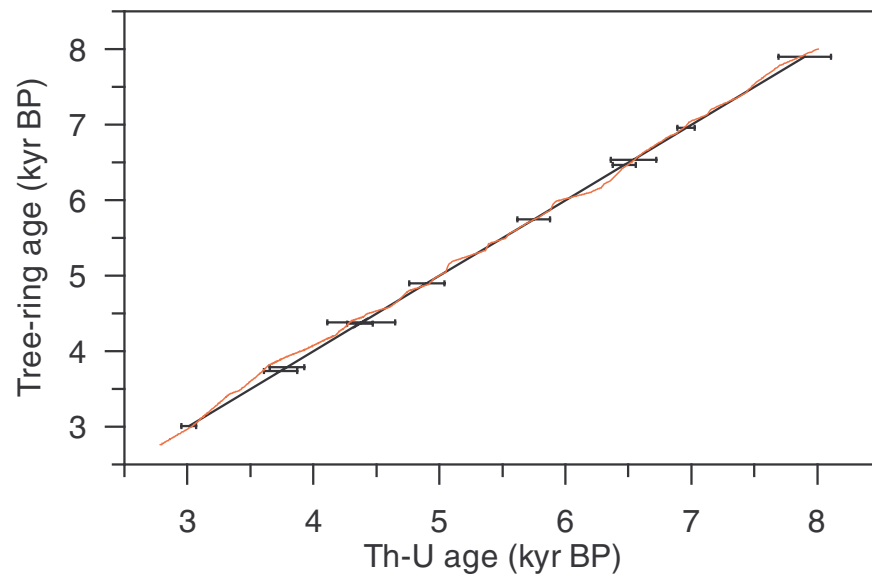


Figure S4. Measured (black line) and optimized (red line) Th-U age scales for stalagmite Q5. The error bars denote the uncertainties of the Th-U ages. The correlation between the time series of $\delta^{18}\text{O}$ and $\Delta^{14}\text{C}_{\text{res}}$ was made using the adjusted Th-U timescale. It is important to note, that the optimized timescale always remains within the uncertainty of the individual Th-U dates.

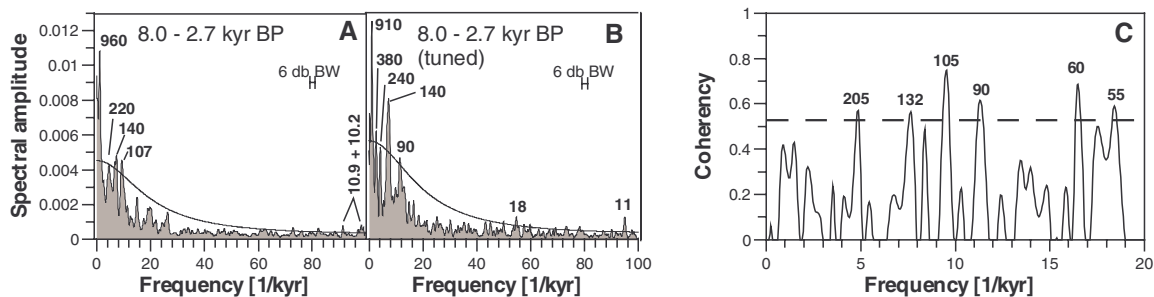


Figure S5. Univariate spectral analyses of the untuned (**A**) and tuned (**B**) $\delta^{18}\text{O}$ time series from stalagmite Q5, and cross-spectral analysis (**C**) of tuned Q5 $\delta^{18}\text{O}$ time series and $\Delta^{14}\text{C}$ measured in tree rings (*S1*) for the time interval up to 8 kyr BP. The Q5 $\delta^{18}\text{O}$ time series were detrended by removing a sinusoid fitted to the late part (see Fig. 1), the polynomial detrended $\Delta^{14}\text{C}$ time series (*S1*) prior to the analyses. The spectra were estimated using the Lomb-Scargle fourier transform for unevenly spaced data, the Welch-Overlapped-Segment-Averaging procedure (5 segments with 50% overlap), linear detrending for each segment, and a Welch I data taper. The univariate spectra (shaded in A and B) were bias-corrected using 2000 Monte-Carlo simulations (*S2*). Shown as red-noise alternative is upper 90% chi-squared bound (smooth line) of a first-order autoregressive (AR1) process. The AR1 process was fitted using the time-domain algorithm of ref *S3* to the $\delta^{18}\text{O}$ time series subsequent to removal of harmonic peaks (> 1000 yr period), yielding an equivalent autocorrelation coefficient of 0.57. This resulted in significant cycles at 960, 220, 140, 107, 10.9, and 10.2 yr period (**A**) and 910, 380, 240, 90, 18, and 11 yr period (**B**). The 6-dB bandwidth (BW), determining the frequency resolution, is 1.06 kyr^{-1} (**A**) and 0.91 kyr^{-1} (**B**, **C**). The coherency spectrum (solid line in **C**), calculated with an alignment of -400 yr of the $\Delta^{14}\text{C}$ time series (*S4*), is compared against the 90% false-alarm-rate level (dashed line), resulting in significant coherent cycles at 205, 132, 105, 90, 60, and 55 yr period (**C**), as well as 32 and 24 yr period (not shown). The univariate spectra were calculated with software REDFIT (*S2*), the bivariate spectrum with SPECTRUM (*S4*); see those papers and references therein for further methodical details.

References for Material and Methods

- S1. M. Stuiver *et al.* *Radiocarbon* **40**, 1041 (1998).
- S2. M. Schulz, M. Mudelsee, *Comput. Geosci.* 28:421 (2002).
- S3. M. Mudelsee, *Comput. Geosci.* **28**, 69 (2002).
- S4. M. Schulz, K. Stattegger, *Comput. Geosci.* **23**:929 (1997).